

# NormalFlow: Fast, Robust, and Accurate Contact-based Object 6DoF Pose Tracking with Vision-based Tactile Sensors

Hung-Jui Huang<sup>1</sup>, Michael Kaess<sup>1</sup>, and Wenzhen Yuan<sup>2</sup>

**Abstract**—Tactile sensing is crucial for robots aiming to achieve human-level dexterity. Among tactile-dependent skills, tactile-based object tracking serves as the cornerstone for many tasks, including manipulation, in-hand manipulation, and 3D reconstruction. In this work, we introduce NormalFlow, a fast, robust, and real-time tactile-based 6DoF tracking algorithm. Leveraging the precise surface normal estimation of vision-based tactile sensors, NormalFlow determines object movements by minimizing discrepancies between the tactile-derived surface normals. Our results show that NormalFlow consistently outperforms competitive baselines and can track low-texture objects like table surfaces. For long-horizon tracking, we demonstrate when rolling the sensor around a bead for 360 degrees, NormalFlow maintains a rotational tracking error of 2.5 degrees. Additionally, we present state-of-the-art tactile-based 3D reconstruction results, showcasing the high accuracy of NormalFlow. We believe NormalFlow unlocks new possibilities for high-precision perception and manipulation tasks that involve interacting with objects using hands. The video demo, code, and dataset are available on our website: <https://joehjhuang.github.io/normalflow>.

## I. INTRODUCTION

The skill to interact with and manipulate objects is fundamental for diverse robotics applications. For effective manipulation, accurate in-hand object tracking is critical, as it enables precise control based on the object’s pose. Although vision-based systems are widely used for object tracking, they often suffer from occlusion during manipulation. OpenAI’s dexterous manipulation system [1] highlights this challenge, as it uses 19 cameras from every angle just to track a block’s rotation in hand. Fortunately, the development of vision-based tactile sensors like GelSight [2] offers a way to accurately track objects without occlusion issues.

In this work, we aim to accurately track objects during contact using vision-based tactile sensors without needing object 3D models. While this capability is the cornerstone of many downstream tasks such as manipulation, in-hand manipulation, and tactile-based 3D reconstruction, the field has not adequately addressed it. Works such as [3] [4] [5] [6] focus on these downstream tasks and handle object tracking by converting tactile images into point clouds and applying registration methods like ICP [7] to determine object transformations. However, these tracking methods often perform poorly with tactile-derived point clouds, which are often noisy and distorted. This issue arises because GelSight and

<sup>1</sup>Hung-Jui Huang and Michael Kaess are with Carnegie Mellon University, Pittsburgh, PA, USA {hungjuih, kaess}@andrew.cmu.edu

<sup>2</sup>Wenzhen Yuan is with University of Illinois Urbana-Champaign, Champaign, IL, USA yuanwz@illinois.edu

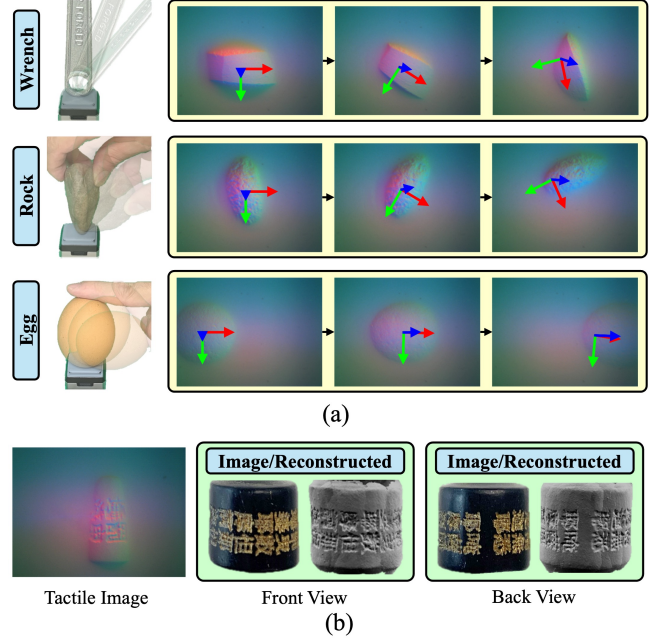


Fig. 1: NormalFlow performs fast, accurate, and robust 6DoF object tracking based on only touch sensing. (a) Accurate tracking of a wide variety of objects, including a wrench, a rock, and even low-texture object like an egg. (b) Applying NormalFlow to tactile-based 3D reconstruction of a 12mm wide bead highlights NormalFlow’s high accuracy.

its variants directly measure surface normals using photometric stereo methods [8], and converting these normals into point clouds requires integration, introducing accumulated noise and distortion. At its core, the field still lacks a fast, accurate, and robust tactile-based tracking solution.

In this paper, we present a novel tactile-based tracking algorithm, NormalFlow, which achieves significantly better robustness and accuracy than existing point cloud registration approaches and runs as fast or faster. Our key insight is to find object transformations by minimizing discrepancies between the surface normal maps of the contact area instead of point clouds. Since derived normal maps are much more accurate for vision-based tactile sensors, this approach yields more precise tracking results. For example, NormalFlow can accurately estimate object rolling angles by computing the rotations of normal vectors, which was previously challenging to estimate for point cloud registration approaches [3]. Inspired by the Lucas-Kanade optical flow method [9], NormalFlow uses Gauss-Newton optimization to minimize

discrepancies between normal maps and determine the 6DoF object pose quickly, robustly, and accurately. Additionally, we propose a robust long-horizon tracking method based on NormalFlow to reduce drifts under extended movements.

We test NormalFlow’s tracking performance on a wide variety of objects and show it consistently outperforms point cloud registration baselines. It achieves an average translation error of 0.29mm (over a total movement of 3.4mm), rotation error of 1.9° (over a total movement of 37.4°), and runs at 70Hz on CPU. NormalFlow can even track objects with low textures, like a flat table surface. For long-horizon tracking, NormalFlow maintains a rotational tracking error of 2.5° after rolling the sensor around a 12mm wide bead for 360°. Additionally, we show NormalFlow’s generalizability across different sensors and resolutions. Finally, to demonstrate NormalFlow’s power, we apply it to tactile-based 3D reconstruction. Leveraging NormalFlow’s high precision, our reconstructed geometry significantly outperforms the geometry reconstructed using motion capture system tracked poses. We believe NormalFlow opens new avenues for higher precision tactile-dependent perception and control.

## II. RELATED WORK

Early methods for tactile-based object pose estimation focused on low-resolution tactile sensors [10], often requiring known 3D object models and numerous tactile readings. Alternatively, most recent approaches [5] [11] [12] utilize high-resolution sensors such as GelSight and its variants [8] [2] [13], achieving more efficient and accurate pose estimation. This review focuses on these recent methods and their achievements in pose estimation tasks.

**Frame-to-Frame Tracking:** Frame-to-frame tracking is to track an object’s movement in the sensor frame using only tactile data. It is the prerequisite for many tactile-dependent tasks [14] [3] [4]. To determine objects’ planar movements in  $SE(2)$ , Li et al. [14] used a feature-based image registration method on tactile-derived height maps, while Sodhi et al. [15] trained a neural network on tactile images. A more important task is determining 6DoF object movement in  $SE(3)$ . Researchers often reduce this problem to registering tactile-derived point clouds or height maps. For instance, [4] [5] [16] used ICP to register point clouds and determine object movements, while [6] performed feature-based point cloud registration before applying ICP. Zhao et al. [3] trained a neural network to predict object transformations from tactile-based height maps. However, these approaches are limited by the often distorted point cloud quality, leading to noisy tracking results and sometimes making rolling movements impossible to estimate [3]. The working principle of vision-based tactile sensors is to use photometric stereo methods to acquire geometrical information [8], specifically through the estimation of surface normals. Deriving point clouds, in this case, by integration of surface normals will result in accumulated noise. Our approach directly measures object movements using the surface normals, leading to more accurate estimations.

**Long-horizon Tracking:** Long-horizon tracking is usually achieved by composing frame-to-frame tracking results, which can introduce drift. To address this, most methods applied factor graph optimization [3] [17]. For example, Sodhi et al. [5] built a factor graph upon the ICP frame-to-frame tracking method, reporting 4 mm translation and 0.2 rad rotation errors when tracking a pyramid-shaped object.

## III. METHOD

We aim to use vision-based tactile sensors to track the 6DoF object poses relative to the sensor’s coordinate frame during contact, without requiring the objects’ geometrical models. Utilizing photometric stereo methods, surface normal maps are derived from the stream of tactile images [16]. The key insight of our NormalFlow algorithm is to find the transformation by directly minimizing discrepancies between normal maps rather than point clouds. This method prevents the accumulated noise associated with the integration process when converting normal maps to point clouds. In contrast, existing approaches [5] [12] used ICP or FilterReg [18] to register point clouds and are prone to noise accumulation.

### A. Surface Geometries Prediction from Tactile Images

Vision-based tactile sensors like GelSight [8] [2] and its derivatives [13] are designed with hardware that employs photometric stereo methods [8] to capture surface normals at each individual pixel from the sensor’s reading. We adapt the approach from [16] to derive surface normal maps from tactile images. The method is chosen for its simplicity, widespread use [3] [6], and accuracy, and can be replaced with alternative approaches [12] [11]. Using the approach in [16], we collect 50 tactile images by pressing a 5mm diameter metal ball against various regions of the sensor’s sensing surface. By manually labeling the circular contact region, we calculate the true surface gradients of each pixel within these regions based on the known ball diameter. A multi-layer perceptron with three hidden layers (5-128-32-32-2) is then trained to learn a mapping from the pixel’s color and position (RGBUV) to its surface gradient ( $g_u, g_v$ ). During test time, the surface normal  $\hat{\mathbf{n}}$  of each pixel is computed from the predicted surface gradient by  $\hat{\mathbf{n}} = \mathbf{n}/\|\mathbf{n}\|$ , where  $\mathbf{n} = [g_u \ g_v \ -1]^T$ .

To derive the height map  $z$ , a 2D fast Poisson solver [2] is applied to integrate the predicted surface gradients. This process accumulates noise and distortion and can hardly be mitigated due to the design choice of the sensor hardware, which directly perceives normals instead of heights. The contact region is straightforwardly determined by regions where the height and tactile image variations exceed a threshold compared to pre-contact conditions.

### B. The NormalFlow Algorithm

Consider a reference sensor frame and a target sensor frame, each characterized by their respective perceived surface normal maps  $\mathbf{I}$  and  $\mathbf{I}'$  as shown in Fig. 2, which are functions  $\mathbb{R}^2 \mapsto \mathbb{R}^3$  mapping pixel coordinates to surface normals. Our goal is to estimate the 6DoF transformation

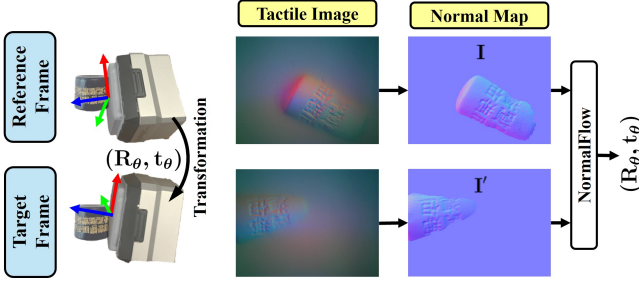


Fig. 2: Given two tactile images before and after object movement, we derive the surface normal maps. NormalFlow determines the object transformations by minimizing discrepancies between the surface normal maps.

from the reference frame to the target frame  $(\mathbf{R}_\theta, \mathbf{t}_\theta) \in SE(3)$ , parameterized as  $\theta = (x, y, z, \theta_x, \theta_y, \theta_z) \in \mathbb{R}^6$ . The NormalFlow algorithm minimizes the difference between two surface maps within the shared contact region: the transformed reference map  $\mathbf{I}$  when applying the 3D transformation to the object, and the target map  $\mathbf{I}'$ . This 3D transformation affects the reference map  $\mathbf{I}$  by rotating the normal directions and re-mapping the pixels. Therefore, the minimization objective of NormalFlow is:

$$\sum_{(u,v) \in \bar{C}} [\mathbf{I}'(\mathbf{W}(u,v;\theta)) - \mathbf{R}_\theta \mathbf{I}(u,v)]^2 \quad (1)$$

where  $(u,v)$  is the pixel coordinates. The shared contact region  $\bar{C}$  is computed as the intersection of the target frame's contact region and the re-mapped contact region in the reference frame. The re-mapping function  $\mathbf{W}(u,v;\theta)$  maps pixel coordinates from the reference frame to the target frame by transforming the 3D surface coordinate of the pixels and projects it to 2D:

$$\mathbf{W}(u,v;\theta) = \mathbf{P}(\mathbf{R}_\theta \cdot \mathbf{q}(u,v) + \mathbf{t}_\theta) \quad (2)$$

where  $\mathbf{q}(u,v) = [u \ v \ z(u,v)]^\top$  is the 3D surface coordinate corresponding to the pixel at  $(u,v)$  in the reference frame and  $\mathbf{P} = \begin{pmatrix} 1 & 0 & 0 \\ 0 & 1 & 0 \end{pmatrix}$  is the projection matrix. Since the indentation is always small ( $z(u,v) \ll u,v$ ), the noise of the height estimation  $z(u,v)$  has minimal impact on the re-mapping function. Inspired by the Lucas-Kanade optical flow method [9] [19], NormalFlow employs the Gauss-Newton optimization to minimize Eq. (1) iteratively. For clarity, we simplify notation by omitting arguments. Linearizing Eq. (1) at the current estimate of  $\theta$  results in:

$$\sum_{(u,v) \in \bar{C}} [(\mathbf{I}'(\mathbf{W}) - \mathbf{R}_\theta \mathbf{I}) + (\nabla \mathbf{I}' \frac{\partial \mathbf{W}}{\partial \theta} - \frac{\partial (\mathbf{R}_\theta \mathbf{I})}{\partial \theta}) \Delta \theta]^2 \quad (3)$$

where  $\nabla \mathbf{I}' = [\frac{\partial \mathbf{I}'}{\partial u} | \frac{\partial \mathbf{I}'}{\partial v}]$  is the gradient normal map evaluated at the re-mapped pixel coordinate  $\mathbf{W}(u,v;\theta)$ . We can further write Eq. (3) in the form of  $\|\mathbf{A} \Delta \theta - \mathbf{b}\|^2$ , representing a linear least square problem. The closed-form solution of it is  $\Delta \theta = \mathbf{H}^{-1} \mathbf{A}^\top \mathbf{b}$ , where  $\mathbf{H} = \mathbf{A}^\top \mathbf{A}$  is the Hessian

matrix. We update the parameters by  $\theta \leftarrow \theta + \Delta \theta$  and repeat the linearization and parameters update process until the parameters converge.

Minimizing discrepancies of the surface normal maps can not resolve the z-translation component of  $\theta$  due to their 2D nature. This limitation stems from the 3D to 2D projection involved in the pixel re-mapping process, which results in the Hessian matrix with zero values for the z-translation dimension. Therefore, we calculate the z-translation independently once the other five dimensions are determined using Gauss-Newton optimization. We do this by computing, within the shared contact region, the mean difference between the target height map and the reference height map transformed using the parameters  $\theta$  determined by the Gauss-Newton optimization:

$$\Delta z = \frac{1}{|\bar{C}|} \sum_{(u,v) \in \bar{C}} [z'(\mathbf{W}) - \mathbf{P}_z(\mathbf{R}_\theta \cdot \mathbf{q} + \mathbf{t}_\theta)] \quad (4)$$

Here,  $z'(\mathbf{W})$  represents the target height map at the re-mapped pixel coordinate, and  $\mathbf{P}_z = \begin{pmatrix} 0 & 0 & 1 \end{pmatrix}$  represents the z-axis projection matrix. We then replace the z-translation dimension in  $\theta$  with the calculated  $\Delta z$  to finalize the transformation estimate. Despite relying on the noisy height map  $z$  and  $z'$ ,  $\Delta z$  estimation errors remain small because  $\Delta z$  itself is always small for the object to maintain contact.

### C. Inverse Composition and Random Subsampling

We employ two techniques to speed up NormalFlow without compromising its performance. During each iteration of the Gauss-Newton optimization, the Hessian matrix  $\mathbf{H}$  is re-evaluated at an updated parameter  $\theta$ . We apply the inverse compositional method [19] to reformulate Eq. (3) so that the Hessian matrix can be pre-computed and re-used for every iteration (see Appendix I). This approach lowers the computational complexity from  $O(nm^2N)$  to  $O(m^2N + nmN)$ , where  $n$  is the number of iterations,  $m = 6$  is the parameter dimension, and  $N$  is the number of pixels in the shared contact region. Additionally, to further reduce runtime, we randomly subsample  $N = 5000$  pixels in the shared contact region from a tactile image resolution of  $320 \times 240$  when evaluating Eq. (3). This choice of  $N$  serves as a conservative lower bound that ensures negligible impact on result quality in practice. Smaller values of  $N$  sometimes still work but offer diminishing returns on runtime reduction.

### D. Long-Horizon Tracking

We propose a keyframe-based approach for long-horizon tracking. Unlike naive approaches that compute transformations relative to the immediately preceding frame and compose these transformations over the horizon, our method computes the transformation from the current frame to the latest keyframe and composes it with the aggregated transformations between keyframes. This technique minimizes drift by reducing the number of transformation composition needed, leveraging the infrequent occurrence of keyframes compared to regular frames. During tracking, if a frame is far from the latest keyframe causing large NormalFlow

estimation errors, it is set as the new keyframe. Specifically, using normal maps  $\mathbf{I}_k$ ,  $\mathbf{I}_p$ , and  $\mathbf{I}_c$  from the latest keyframe, previous, and current frames, we estimate transformations via NormalFlow. We calculate  ${}^c\mathbf{T}_k$  between the latest keyframe and current frame, and  ${}^c\mathbf{T}_p$  between the previous and current frames. If the difference between  $({}^c\mathbf{T}_p)^{-1} \cdot {}^c\mathbf{T}_k$  and  ${}^p\mathbf{T}_k$  (estimated in the previous time step) exceeds a threshold, we set the previous frame as the new keyframe. To further reduce drift, factor graph optimization [5] can be built upon our approach; however, this is beyond the scope of our paper.

### E. Discussion and Comparison

For math completeness, our NormalFlow derivation uses the noisy height map. In fact, the noise’s effect on NormalFlow is minimal. In practice, skipping height map computation by simply assuming a zero height map ( $z(u, v) = 0$ ) has a minor effect on NormalFlow’s estimation error and still significantly outperforms the point cloud registration methods (See Section IV-A.3 for ablation results).

Next, we discuss the advantages of using surface normals (NormalFlow) for pose estimation over point clouds (ICP). Consider determining the tilt of a flat surface. The rotations of surface normals directly reveal the tilt, whereas estimating tilt using distorted point clouds can be noisy. For a textured ball, pose estimation should rely on the textures. Unfortunately, ICP will focus on registering the global ball shape since the textures minimally affect point locations. In contrast, NormalFlow will estimate pose from textures by matching the diverse normal directions in the textured region.

## IV. EXPERIMENTS AND RESULTS

In this section, we perform experiments to evaluate the accuracy and speed of the NormalFlow method for tracking the motion of different objects. We also evaluate the effect of object movement speed on tracking performance and the method’s generalizability with different tactile sensors and sensor resolutions. Unless specified, all experiments are conducted on the GelSight Mini sensor with a resized resolution of  $320 \times 240$ . This sensor has a  $20\text{mm} \times 15\text{mm}$  sensing area and operates at 25 Hz.

### A. Object 6DoF Pose Tracking

In this experiment, we evaluate the tracking accuracy and runtime of NormalFlow against baseline methods on various objects and show its long-horizon tracking performance.

1) *Data Collection*: To evaluate our approach, we collect pose tracking data on 12 objects in three categories: seven everyday objects (four from the YCB dataset [20]), two small textured objects, and three simple geometric shapes (Fig. 5). We clamp the objects on a fixed table and mount the GelSight Mini on a movable plate tracked by the OptiTrack motion capture system (MoCap) to capture the ground truth sensor poses (Fig. 3). For each object, we collect seven tracking data trials, initiating contact at different poses shown in Fig. 4. To prevent quick damage to the Gel, which is very vulnerable to wearing under pure sliding actions, we mainly apply rotational movements on the object’s surface, including

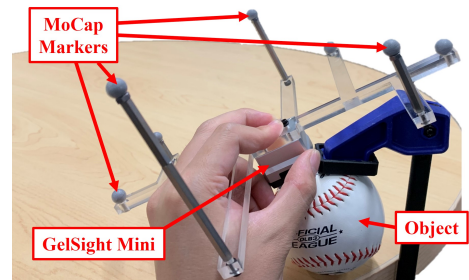


Fig. 3: The data collection setup, with the object clamped on the table and the GelSight sensor tracked by MoCap.

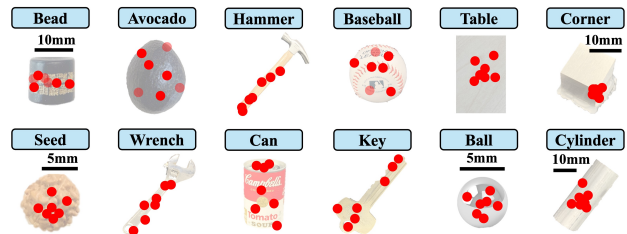


Fig. 4: Initial contact locations (manually labeled) for the seven trials per object in the tracking experiment.

rolling in the x-y plane and twisting along the z-axis. By changing the rotation center, rotational movements can cause object translations. Our data collection process includes these translations to demonstrate our approach’s effectiveness in tracking object movements in all 6DoF. For each trial, we maintain the object’s position not too far from its initial pose to ensure sufficient overlap in the contact area relative to the initial frame, thereby avoiding setting new keyframes. On average, each trial includes 10.2sec of tracking data, and the average 6DoF moving range is shown in Table I.

x(mm)	y(mm)	z(mm)	$\theta_x(^{\circ})$	$\theta_y(^{\circ})$	$\theta_z(^{\circ})$
2.30	2.30	1.11	16.2	18.0	28.5

TABLE I: Dataset statistics: average 6DoF moving range.

2) *Baseline Methods*: We compare NormalFlow with three common point cloud registration methods. For each tactile image, we convert the predicted height map  $z$  into a point cloud, excluding points outside the predicted contact region, which then serves as input for these baseline methods: **Point-to-Plane ICP** [7]: Referred to as ICP in this paper, Point-to-plane ICP is a local registration approach and is commonly used for tactile-based tracking [16] [5] [4]. We utilize the implementation from the Open3D Library [21]. **FilterReg** [18]: FilterReg is a probabilistic local point cloud registration approach. It is more robust than ICP and has been applied in [22] for tactile registration. We utilize the implementation from the ProbReg Library [23]. **FPFH + RANSAC + ICP**: Abbreviated as FPFH+RI in this paper, it combines Fast Point Feature Histograms (FPFH) [24] and RANSAC to extract features and register point clouds globally. It then applies ICP to refine the alignment. The approach is applied in [6] for tactile registration. We

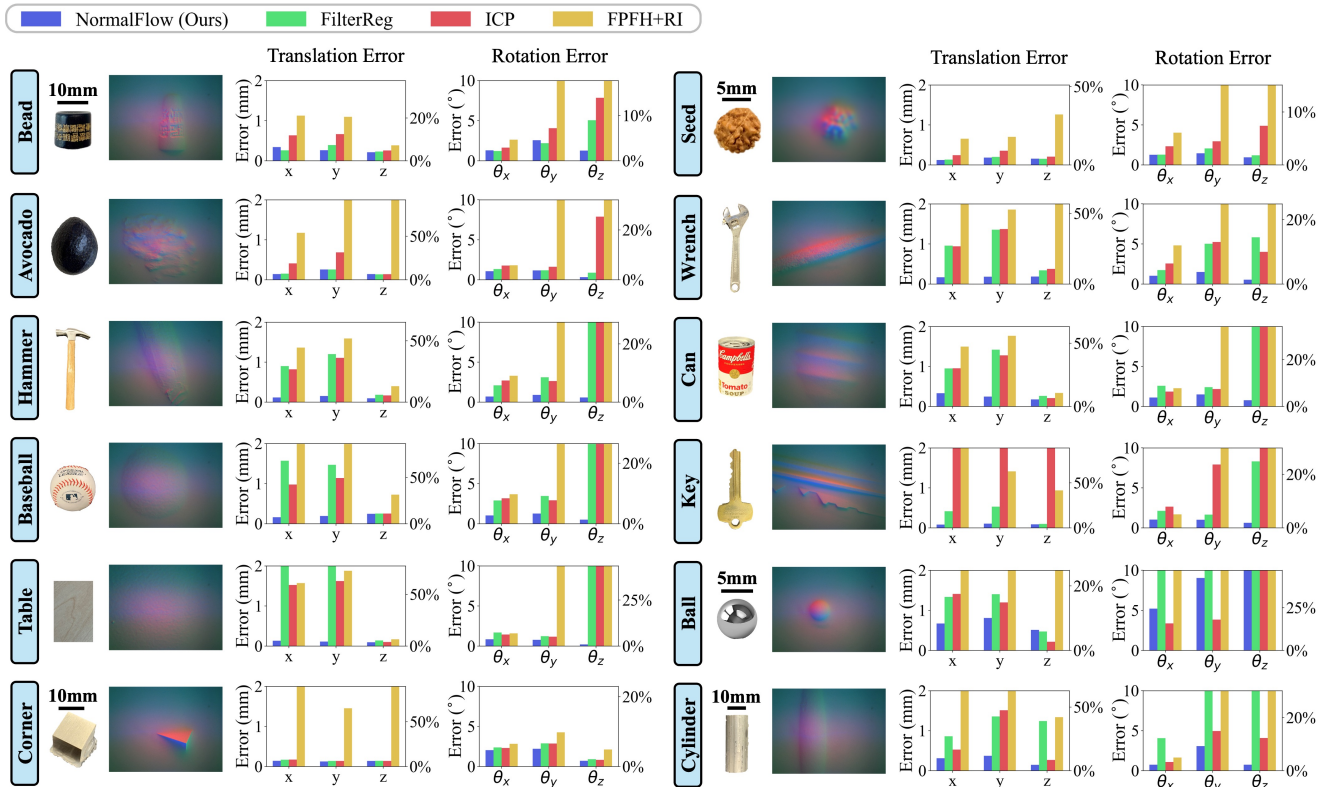


Fig. 5: Tracking results for the 12 objects. For each object: **[left]** the object (scale not shown for common objects) and a sample tactile image (Seed’s image slightly blurred to avoid visualization discomfort); **[right]** the 6DoF tracking MAE: left y-axis shows absolute error, right y-axis shows percentage error relative to object movement range.

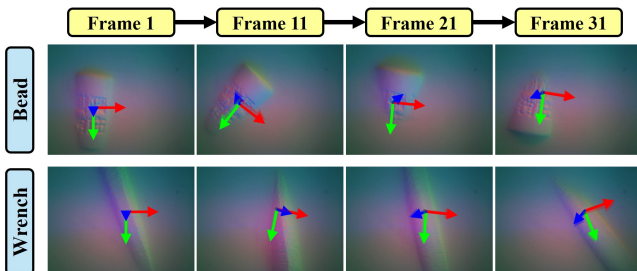


Fig. 6: Example trials on two objects. RGB axes show NormalFlow estimated poses. Transparent RGB axes show MoCap poses, nearly overlapping with NormalFlow poses.

utilize the implementation from the Open3D Library [21].

The local registration methods (NormalFlow, ICP, and FilterReg) are initialized using the pose estimated from the previous frame.

3) *Tracking Results*: For all methods, we estimate and evaluate the 6DoF sensor pose mean absolute error (MAE) for each frame relative to the first frame. The tracking result is shown in Fig. 5, with rotation angles in the z-x-y Euler format. Two example tracking trials using NormalFlow are shown in Fig. 6. NormalFlow outperforms baselines on all objects, particularly objects with less textures. We observe that all methods struggled with perfectly symmetrical objects (Ball and Cylinder) due to ambiguities in matching normal

maps or point clouds. Excluding these two objects, the average tracking error is shown in Table II. Note that the translational tracking error of MoCap (ground truth) is about 0.2mm. We find that FPFH+RI often falls into local minima, explaining the challenges of extracting features from tactile point clouds. Meanwhile, ICP consistently performs worse than NormalFlow and FilterReg. While NormalFlow only slightly exceeds FilterReg’s performance on highly textured objects (like Avocado and Seed), it significantly outperforms FilterReg on less textured objects (like Wrench and Hammer) by maintaining robust tracking where FilterReg often fails. To the extreme, NormalFlow can robustly track objects like Table, which is considered textureless by human standards.

**Ablation Study**: To demonstrate NormalFlow’s resilience to height estimation errors, we conduct an ablation study by rerunning NormalFlow without height information (assuming a zero height map). The results show only minor changes in 6DoF tracking performance (Table II), with MAE values of 0.19mm, 0.18mm, and 0.18mm for x, y, and z translations, and  $1.2^\circ$ ,  $1.57^\circ$ , and  $0.69^\circ$  for  $\theta_x$ ,  $\theta_y$ , and  $\theta_z$  rotations.

4) *Runtime Analysis*: In all experiments, we randomly subsample  $N = 5000$  pixels when running NormalFlow (Section III-C). For a fair runtime comparison in this subsection, we similarly subsample  $N = 5000$  points in the point cloud for the baseline algorithms. Note that, unlike here, the baselines in all other subsections run using the full point

Method	x(mm)	y(mm)	z(mm)	$\theta_x(^{\circ})$	$\theta_y(^{\circ})$	$\theta_z(^{\circ})$
NormalFlow	<b>0.17</b>	<b>0.18</b>	<b>0.15</b>	<b>1.13</b>	<b>1.42</b>	<b>0.64</b>
FilterReg	0.85	1.05	0.20	1.96	2.59	15.4
ICP	1.22	3.44	0.85	2.27	3.30	15.9
FPFH+RI	2.38	1.69	1.26	2.93	36.8	27.8

TABLE II: 6DoF tracking MAE for all objects, excluding the two perfectly symmetrical objects (Ball and Cylinder).

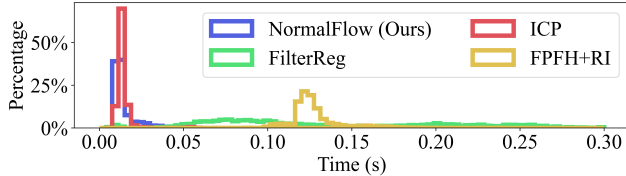


Fig. 7: The runtime histogram. The average runtimes are: NormalFlow (13.9 ms), ICP (13.6 ms), FilterReg (145 ms), and FPFH+RI (127 ms).

cloud. All algorithms are tested on a laptop equipped with an AMD Ryzen 7 PRO 7840U CPU without GPU acceleration. The runtime histograms are shown in Fig. 7. The average runtime of NormalFlow is 13.9 ms, closely comparable to ICP at 13.6 ms, and significantly faster than FilterReg at 145 ms and FPFH+RI at 127 ms.

5) *Long-horizon Tracking Results*: We demonstrate the long-horizon tracking performance of our approach using three objects with varying tracking difficulty: Bead (easy), Wrench (medium), and Table (hard). For each object, we conduct a trial where the sensor travels a significant distance from its initial pose, requiring multiple keyframes during the tracking process. The NormalFlow tracking results (Fig. 8) indicate minimal tracking error even after extensive movement. After rolling the Bead 360 degrees along the y-axis and twisting it 540 degrees along the z-axis, the tracking errors in the y-axis and z-axis remain 2.5 and 1.8 degrees, respectively. Note that determining rolling angles along the y-axis has been previously considered challenging [3]. While minor drift occurs, future work can correct it with a factor graph layer [5], with NormalFlow providing more accurate between-factor estimates than conventional ICP methods.

6) *Tracking by Sliding*: Although pure sliding objects on the sensor are discouraged as they wear the Gel quickly, we conducted this experiment to show that NormalFlow can track well under pure sliding. We test the tracking performance under pure sliding with two easily slidable objects: Bead and Wrench. Seven trials were conducted for each object, with an average sliding distance of 13.2 mm for the Bead and 13.1 mm for the Wrench, reaching the distance limit without setting new keyframes. The 6DoF tracking MAE of NormalFlow and baselines are shown in Fig. 9. The results show that NormalFlow tracks effectively under pure sliding and outperforms the baseline methods.

### B. Movement Tolerance for Tracking

When the object moves too quickly, NormalFlow may initialize far from the true pose, causing tracking failures.

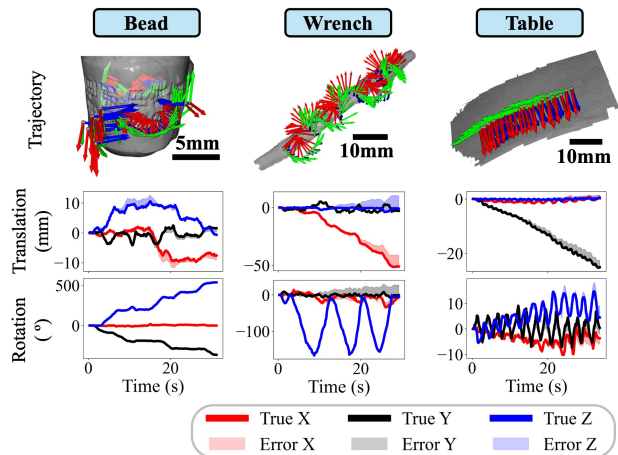


Fig. 8: Long-horizon tracking results. For each column: **[top]** sensor trajectories with poses as RGB coordinate axes; **[bottom]** true 6DoF sensor movements tracked by MoCap (solid lines) and NormalFlow estimation error (shaded area), which is often too small to be seen.

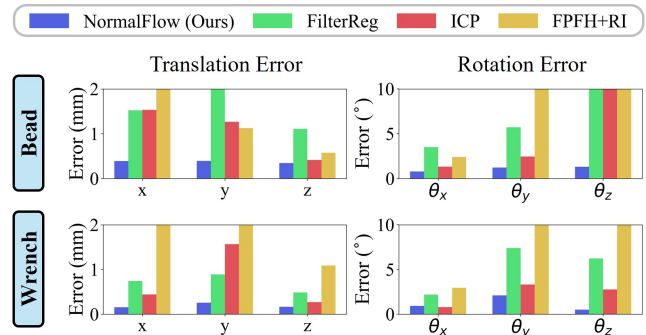


Fig. 9: 6DoF tracking MAE under pure sliding.

We evaluate the maximum object moving speed NormalFlow can track by analyzing its region of convergence—the range of pose initialization from which tracking succeeds—using three objects with varying tracking difficulty: Seed (easy), Wrench (medium), and Table (hard). The Wrench is touched and tracked at the neck. For each object, we conduct a trial, with each tactile image testing 2000 initial conditions based on the true pose with added shifts. Of these shifts, 1000 involves rotations evenly sampled within  $\pm 60^{\circ}$  across all axes, and 1000 involves translations evenly sampled within  $\pm 2$  mm across all axes. Fig. 10 shows the convergence rate for different initializations, with Table having the smallest region of convergence. We speculate that objects with less symmetrical global geometry, like Wrench, have a larger region of convergence. On average, NormalFlow tracks Table effectively as long as translational movements between frames stay below 1.39 mm (34.8 mm/s) and rotational movements below  $40.1^{\circ}$  (17.5 rad/s). This result shows that NormalFlow is robust to fast rotation but less so to fast translation, which is usually not an issue since fast translation wears the Gel quickly and should be avoided.

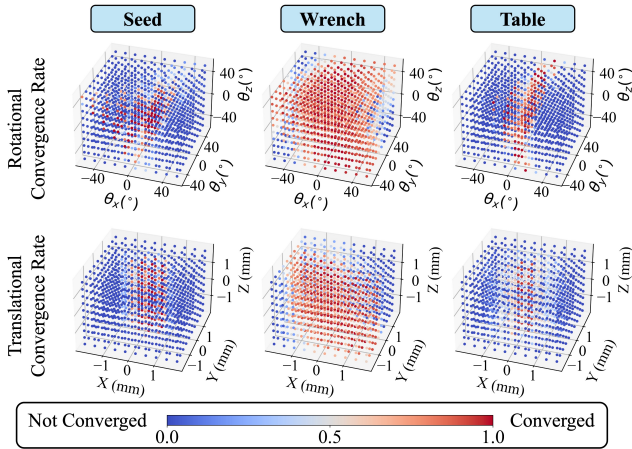


Fig. 10: Convergence rate for different initialization conditions for the three objects. NormalFlow tracks well when object movement between frames is in the red region.

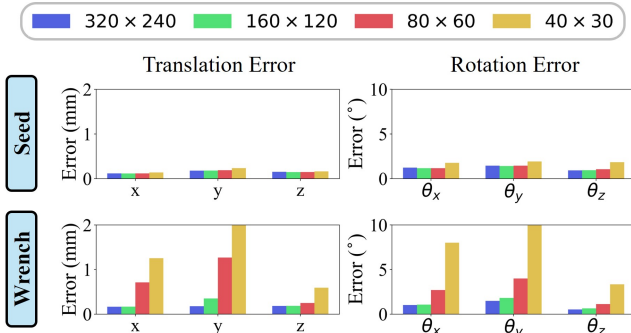


Fig. 11: Effect of spatial resolution on tracking accuracy.

### C. Resolution Comparison

We analyze how sensor spatial resolution affects tracking accuracy. Fig. 11 shows the tracking MAE for Seed and Wrench when using downsampled tactile images. Accurate tracking is maintained with 2x downsampling, but lower resolution degrades performance for Wrench (less textured).

### D. Tracking Performance on DIGIT

We demonstrate our approach using the DIGIT sensor [13]. GelSight Mini and DIGIT are the two most common off-the-shelf vision-based tactile sensors. DIGIT has a resolution of  $640 \times 480$ , a  $13\text{mm} \times 9.7\text{mm}$  sensing area, and operates at 60 Hz. Compared to GelSight Mini, DIGIT’s blurrier images with less texture detail result in less accurate shape and normal estimation. Using the setup described in Section IV-A.1, we collect tracking data on Seed and Wrench with 7 trials each. Fig. 12 shows the 6DoF tracking MAE using all methods. NormalFlow outperforms all baselines, though less so on Wrench due to DIGIT’s texture loss.

## V. APPLICATION: TACTILE-BASED 3D RECONSTRUCTION

We demonstrate the power of NormalFlow by applying it to the task of tactile-based 3D reconstruction. Here, we

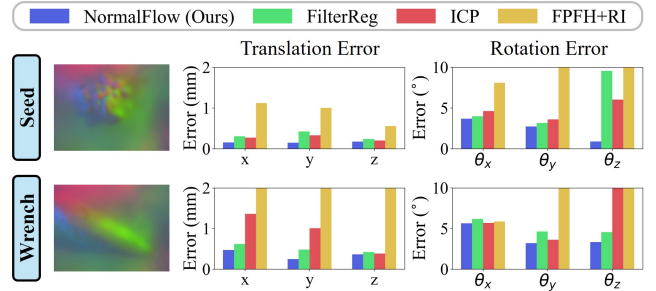


Fig. 12: DIGIT tracking results for Seed and Wrench. [left] Sample tactile images; [right] 6DoF tracking MAE.

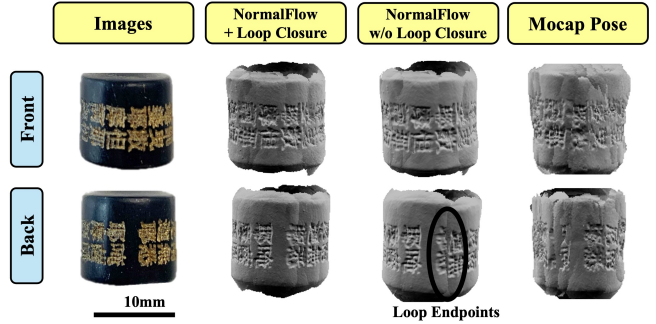


Fig. 13: Comparison of tactile-based 3D reconstruction of the Bead using NormalFlow estimated poses (with and without loop closure) versus MoCap tracked poses. The Bead is rolled on GelSight (trajectory shown in Fig. 8) to capture a tactile video for reconstruction. See the supplementary video for the dynamic process.

reconstruct the Bead, which poses challenges for vision-based methods due to its carved texture being mistaken for painted texture. We manually roll the Bead on GelSight Mini without breaking contact to collect a tactile video, with each frame revealing a small portion of the Bead (Fig. 6). Using NormalFlow, we track the 6DoF sensor pose of each frame and set new keyframes as needed. Upon completing a full rotation and returning near the initial pose, we perform loop closure by identifying the frame closest to the initial pose. NormalFlow is then used to determine the relative pose between this frame and the initial one. Finally, we estimate the poses of all frames by optimizing the pose graph with this single loop, setting covariances identically across all factors.

Fig. 13 compares three reconstructions of the Bead using local meshes from individual frames registered to NormalFlow poses (both with and without loop closure) and MoCap-tracked poses. The reconstruction result using NormalFlow estimated poses qualitatively outperforms the one using MoCap. This experiment highlights the accuracy of NormalFlow, demonstrating that even with naive pose graph optimization, NormalFlow achieves significantly better 3D reconstruction results compared to previous methods like [3].

## VI. CONCLUSION

In this work, we present NormalFlow, a fast, robust, and accurate 6DoF pose tracking algorithm for vision-based

tactile sensors. By directly minimizing discrepancies between surface normal maps instead of point clouds, our approach outperforms baseline methods and tracks well even with low-texture objects. We also evaluate the effects of object movement speed, sensor choice, and sensor resolution on tracking performance. Finally, we demonstrate the effectiveness of NormalFlow in tactile-based 3D reconstruction. However, NormalFlow is not prone to limitations. NormalFlow can lose track during fast sliding movements (Section IV-B). Simple fixes include initializing NormalFlow with the translation component of the transformation using ICP results or the shift of the contact region’s center. We believe NormalFlow can be widely applied, enabling new advancements for high-precision perception, control, and manipulation tasks.

## REFERENCES

- [1] O. M. Andrychowicz, B. Baker, M. Chocie, R. Józefowicz, B. McGrew, J. Pachocki, A. Petron, M. Plappert, G. Powell, A. Ray, J. Schneider, S. Sidor, J. Tobin, P. Welinder, L. Weng, and W. Zaremba, “Learning dexterous in-hand manipulation,” *The International Journal of Robotics Research*, vol. 39, no. 1, pp. 3–20, 2020.
- [2] W. Yuan, S. Dong, and E. H. Adelson, “Gelsight: High-resolution robot tactile sensors for estimating geometry and force,” *Sensors*, vol. 17, no. 12, 2017.
- [3] J. Zhao, M. Bauza, and E. H. Adelson, “Fingerslam: Closed-loop unknown object localization and reconstruction from visuo-tactile feedback,” 2023.
- [4] S. Suresh, H. Qi, T. Wu, T. Fan, L. Pineda, M. Lambeta, J. Malik, M. Kalakrishnan, R. Calandra, M. Kaess, J. Ortiz, and M. Mukadam, “Neural feels with neural fields: Visuo-tactile perception for in-hand manipulation,” 2023.
- [5] P. Sodhi, M. Kaess, M. Mukadam, and S. Anderson, “Patchgraph: In-hand tactile tracking with learned surface normals,” in *2022 International Conference on Robotics and Automation (ICRA)*. IEEE Press, 2022, p. 2164–2170.
- [6] J. Lu, Z. Wan, and Y. Zhang, “Tac2structure: Object surface reconstruction only through multi times touch,” *IEEE Robotics and Automation Letters*, vol. 8, no. 3, pp. 1391–1398, 2023.
- [7] Y. Chen and G. G. Medioni, “Object modeling by registration of multiple range images,” *Proceedings. 1991 IEEE International Conference on Robotics and Automation*, pp. 2724–2729 vol.3, 1991.
- [8] M. K. Johnson, F. Cole, A. Raj, and E. H. Adelson, “Microgeometry capture using an elastomeric sensor,” *ACM Trans. Graph.*, vol. 30, no. 4, jul 2011.
- [9] B. D. Lucas and T. Kanade, “An iterative image registration technique with an application to stereo vision,” in *Proceedings of the 7th International Joint Conference on Artificial Intelligence - Volume 2*, ser. IJCAI’81. San Francisco, CA, USA: Morgan Kaufmann Publishers Inc., 1981, p. 674–679.
- [10] A. Petrovskaya and O. Khatib, “Global localization of objects via touch,” *IEEE Transactions on Robotics*, vol. 27, no. 3, pp. 569–585, 2011.
- [11] S. Suresh, Z. Si, S. Anderson, M. Kaess, and M. Mukadam, “Midas-Touch: Monte-Carlo inference over distributions across sliding touch,” in *Proc. Conf. on Robot Learning, CoRL*, Auckland, NZ, Dec. 2022.
- [12] M. Bauza, A. Bronars, and A. Rodriguez, “Tac2pose: Tactile object pose estimation from the first touch,” *The International Journal of Robotics Research*, vol. 42, no. 13, pp. 1185–1209, 2023.
- [13] M. Lambeta, P. wei Chou, S. Tian, B. Yang, B. Maloon, V. R. Most, D. Stroud, R. Santos, A. Byagowi, G. Kammerer, D. Jayaraman, and R. Calandra, “Digit: A novel design for a low-cost compact high-resolution tactile sensor with application to in-hand manipulation,” *IEEE Robotics and Automation Letters*, vol. 5, pp. 3838–3845, 2020.
- [14] R. Li, R. Platt, W. Yuan, A. ten Pas, N. Roscup, M. A. Srinivasan, and E. Adelson, “Localization and manipulation of small parts using gelsight tactile sensing,” in *2014 IEEE/RSJ International Conference on Intelligent Robots and Systems*, 2014, pp. 3988–3993.
- [15] P. Sodhi, M. Kaess, M. Mukadam, and S. Anderson, “Learning tactile models for factor graph-based estimation,” in *2021 IEEE International Conference on Robotics and Automation (ICRA)*, 2021, pp. 13 686–13 692.
- [16] S. Wang, Y. She, B. Romero, and E. H. Adelson, “Gelsight wedge: Measuring high-resolution 3d contact geometry with a compact robot finger,” in *2021 IEEE International Conference on Robotics and Automation (ICRA)*. IEEE, 2021.
- [17] S. Kim, A. Bronars, P. Patre, and A. Rodriguez, “Texterity – tactile extrinsic dexterity: Simultaneous tactile estimation and control for extrinsic dexterity,” 2024.
- [18] W. Gao and R. Tedrake, “Filterreg: Robust and efficient probabilistic point-set registration using gaussian filter and twist parameterization,” in *2019 IEEE/CVF Conference on Computer Vision and Pattern Recognition (CVPR)*, 2019, pp. 11 087–11 096.
- [19] S. Baker and I. Matthews, “Lucas-kanade 20 years on: A unifying framework,” *International Journal of Computer Vision*, vol. 56, no. 3, pp. 221 – 255, March 2004.
- [20] B. Calli, A. Singh, J. Bruce, A. Walsman, K. Konolige, S. Sriniyasa, P. Abbeel, and A. M. Dollar, “Yale-cmu-berkeley dataset for robotic manipulation research,” *The International Journal of Robotics Research*, vol. 36, no. 3, pp. 261–268, 2017.
- [21] Q.-Y. Zhou, J. Park, and V. Koltun, “Open3D: A modern library for 3D data processing,” *arXiv:1801.09847*, 2018.
- [22] M. Bauzá, E. Valls, B. Lim, T. Sechopoulos, and A. Rodriguez, “Tactile object pose estimation from the first touch with geometric contact rendering,” in *Conference on Robot Learning*, 2020.
- [23] Kenta-Tanaka et al., “probreg,” 2019. [Online]. Available: <https://probreg.readthedocs.io/en/latest/>
- [24] R. B. Rusu, N. Blodow, and M. Beetz, “Fast point feature histograms (fpfh) for 3d registration,” in *2009 IEEE International Conference on Robotics and Automation*, 2009, pp. 3212–3217.

## APPENDIX I

### INVERSE COMPOSITIONAL FORMULATION

Instead of directly linearizing Equation (1), we apply the inverse compositional formulation [19] by considering a small transformation  $\Delta\theta$ . We optimize  $\Delta\theta$  by minimizing discrepancies between two transformed normal maps: the reference map transformed by the current estimate  $\theta$ , and the target map transformed by  $\Delta\theta$ . The objective is:

$$\sum_{(u,v) \in \bar{C}} \left[ \mathbf{R}_{\theta}^{-1} \mathbf{I}'(\mathbf{W}(u, v; \theta)) - \mathbf{R}_{\Delta\theta}^{-1} \mathbf{I}(\mathbf{W}(u, v; \Delta\theta)) \right]^2 \quad (5)$$

where  $\mathbf{R}_{\Delta\theta}$  is the small rotation matrix parameterized with  $\Delta\theta$ . The first-order Taylor expansion on Equation (5) yields:

$$\sum_{(u,v) \in \bar{C}} \left[ \left( \mathbf{R}_{\theta}^{-1} \mathbf{I}'(\mathbf{W}(u, v; \theta)) - \mathbf{I}(u, v) \right) - \mathbf{J} \Delta\theta \right]^2 \quad (6)$$

Here,  $\mathbf{J}$  represents the first-order terms of Taylor expansion and can be presented in closed-form:

$$\mathbf{J} = \nabla \mathbf{I}(u, v) \cdot \mathbf{P} \cdot \begin{bmatrix} \mathbf{I}_{3 \times 3} & \mathbf{J}_x \mathbf{q} & \mathbf{J}_y \mathbf{q} & \mathbf{J}_z \mathbf{q} \end{bmatrix} - \begin{bmatrix} \mathbf{0}_{3 \times 3} & \mathbf{J}_x \mathbf{I} & \mathbf{J}_y \mathbf{I} & \mathbf{J}_z \mathbf{I} \end{bmatrix} \quad \text{where}$$

$$\mathbf{J}_x = \begin{bmatrix} 0 & 0 & 0 \\ 0 & 0 & -1 \\ 0 & 1 & 0 \end{bmatrix} \quad \mathbf{J}_y = \begin{bmatrix} 0 & 0 & 1 \\ 0 & 0 & 0 \\ -1 & 0 & 0 \end{bmatrix} \quad \mathbf{J}_z = \begin{bmatrix} 0 & -1 & 0 \\ 1 & 0 & 0 \\ 0 & 0 & 0 \end{bmatrix}$$

Independent to the current estimate  $\theta$ , the matrix  $\mathbf{J}$  and the computationally intensive Hessian matrix  $\mathbf{H}$  can now be pre-computed and re-used in every iteration of the Gauss-Newton optimization, significantly reducing the algorithm’s runtime. Finally, we employ the inverse compositional rule to update the current estimate:  $\theta \leftarrow \theta \circ \Delta\theta^{-1}$  [19].